




Excitation of localized graphene plasmons by a metallic slitYu. V. Bludov ^{1,*}, N. M. R. Peres ^{1,2} and M. I. Vasilevskiy ^{1,2}¹*Department of Physics, Center of Physics, and QuantaLab, University of Minho, Campus of Gualtar, 4710-057 Braga, Portugal*²*International Iberian Nanotechnology Laboratory (INL), Avenida Mestre José Veiga, 4715-330 Braga, Portugal*

(Received 26 June 2019; revised manuscript received 24 January 2020; accepted 24 January 2020; published 12 February 2020)

In this paper we show that graphene surface plasmons can be excited when an electromagnetic wave packet impinges on a single metal slit covered with graphene. The excitation of the plasmons localized over the slit is revealed by characteristic peaks in the absorption spectrum. It is shown that the position of the peaks can be tuned either by the graphene doping level or by the dielectric function of the material filling the slit. The whole system forms the basis for a plasmonic sensor when the slit is filled with an analyte.

DOI: [10.1103/PhysRevB.101.075415](https://doi.org/10.1103/PhysRevB.101.075415)**I. INTRODUCTION**

The diffraction of electromagnetic (EM) waves on metallic structures gives rise to a series of interesting phenomena, such as the Wood and Rayleigh anomalies [1,2] and the extraordinary optical transmission [3]. Theoretical models for these phenomena have been elaborated by modeling the metal as a perfect electric conductor (PEC), as in Refs. [4–6]. One of the fundamental problems in the nano-optics is the diffraction of light on a single slit of subwavelength width perforated in a metal. This kind of diffraction is accompanied by a series of effects such as funneling of the EM energy into the slit [7,8] and field enhancement inside it [7], Fabri-Pérot resonances across the metallic film [9–11], transmittance oscillations with an incidence angle variation in the geometrical optics limit [12] and its absence in the subwavelength limit [11], and the sensitivity of the transmittance resonance frequencies to the refractive index of the material inside the slit [11].

Consideration of the light diffraction on a single slit in real metals [13–15], with surface capable of supporting surface plasmon polaritons (SPPs) enriches considerably the physics of the diffraction phenomena [16]. Nevertheless, SPPs in noble metals suffer from relatively high losses in the visible light wavelength, which considerably shorten their mean free path. One of the ways to overcome this difficulty is to use graphene plasmons that can be combined with other materials in order to modify SPP's properties [17–22].

As is well known, SPPs in graphene possess both a large lifetime and a high degree of field confinement [23,24]. This property implies the advantage of using some kind of hybrid metal-graphene structures, where graphene sustains the propagation of SPPs, while PEC modifies their dispersion properties. For example, screening of graphene SPPs by a perfect [25–27] or dispersive (Drude) [28] metal adjacent to it leads to the formation of acoustic SPPs with linear spectrum. Moreover, in such kind of structures SPP's group velocity is quite low compared to polaritons in graphene on a thick

dielectric substrate since high wave vectors correspond to relatively low frequencies in the SPP dispersion relation. The latter means that graphene's conductivity exhibits its nonlocal properties in the THz frequency range and, therefore, gives rise to the nonlocal SPPs [29–32]. Simultaneously, graphene's conductivity (and, consequently, the dispersion properties of SPPs) can be effectively controlled by changing the applied gate voltage [33], which allows one to achieve the dynamical tunability of the resonant frequency in the graphene-based structures [34–38]. Being combined with a metallic grating, a variation of gate voltage permits us to control spoof plasmons [39].

Since the dispersion properties of SPPs are extremely sensitive to the dielectric constant of the surrounding medium, plasmonics structures are widely used for molecular and biosensing [40]. The use of graphene in plasmonic biosensors [41,42] has an additional advantage, since the above-mentioned tunability of the plasmonic resonance frequency allows for us to achieve it in the spectral range where the strength of the characteristic molecular signal is the highest [43].

Monochromatic plane waves are idealizations that, strictly speaking, never occur in reality. The electromagnetic wave that impinges on the plasmonic structure and couples to SPPs (if the necessary conditions are fulfilled [17]), generally is a wave packet, i.e., a superposition of plane waves with close but unequal frequencies and wave vectors, which may represent either a pulse or a focused beam [44]. In the present paper, we consider the diffraction of a localized wave packet (focused beam) on a single rectangular slit in a PEC film, which is covered by a graphene sheet encapsulated (that is, cladded) by two hBN layers at one side and open on the other side (see Fig. 1). We demonstrate that an electromagnetic wave constituting the packet, when diffracted by the slit edges, excites a standing wave of SPPs in graphene at a series of resonant frequencies, which are determined by the graphene doping. At these resonance frequencies, the slit width contains an integer number of SPP wavelengths. Excitation of the polaritons yields a series of absorption peaks in the spectrum and these resonant frequencies turn out to be very sensitive to

*bludov@fisica.uminho.pt

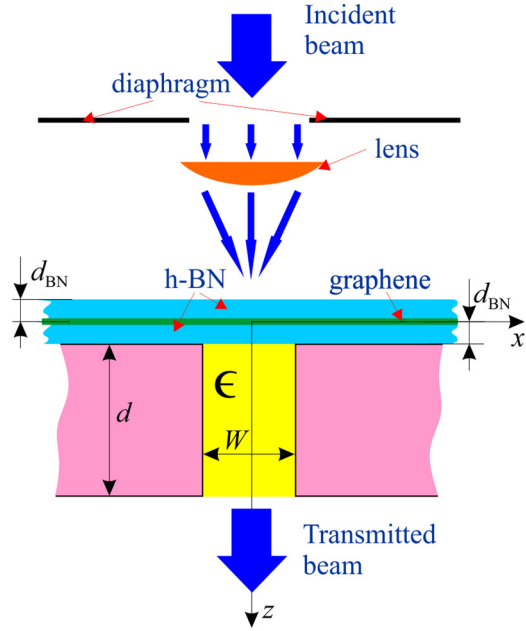


FIG. 1. Single slit (yellow) in the metal film (pink), covered with hBN-encapsulated graphene layer. Also shown are the coordinate axes and the proposed scheme for the obtaining of focused beam by means of diaphragm and cylindric lens.

the dielectric constant of the dielectric material filling the slit, as will be demonstrated by our calculated results.

The paper is organized as follows. In Sec. II we present the solution of Maxwell's equations in the structure and derive the equations for the amplitudes of the eigenmodes. Section III is devoted to the diffraction of the wave packet on the graphene monolayer suspended on top of the slit. In Sec. IV we describe the features of the wave packet's diffraction on the slit covered by an hBN—graphene—hBN layered structure as well as its potential application in sensing. Conclusion are presented in Sec. V.

II. PROBLEM STATEMENT AND MAIN EQUATIONS

A. Structure

We consider a graphene monolayer, located at the plane $z = 0$ and deposited on top of a hBN layer of thickness d_{BN} that occupies the spatial domain $0 < z < d_{\text{BN}}$. The graphene sheet is covered by another hBN layer of the same thickness ($-d_{\text{BN}} < z < 0$). The lower hBN layer is deposited on top of the PEC film of thickness d (see Fig. 1) with the surfaces located at $z = d_{\text{BN}}$ and $z = d_{\text{BN}} + d$. The PEC film contains the single rectangular slit of width W ($-W/2 < x < W/2$), filled with a dielectric with the permittivity ϵ . We consider the incident wave packet propagating in the positive z -axis direction, localized in the x direction and impinging on the uppermost hBN layer at normal incidence. Furthermore, it is essential that the wave packet is described by an even amplitude function of x with respect to the vertical symmetry plane $x = 0$. To simplify the calculations, we shall consider the wave packet of a constant amplitude within a certain range of k_x , $|k_x| \leq k_c$, where $k_c \leq \omega/c$, ω is the frequency, and c is the velocity of light in vacuum.

B. Maxwell equations and their solutions

Since the system under consideration is homogeneous in the direction y (i.e., $\partial/\partial y \equiv 0$), the Maxwell equations can be decoupled into two subsystems, which govern TM- and TE-polarized waves. In the following we will consider the case of TM-polarized waves only, which have the field components $\mathbf{E} = (E_x, 0, E_z)$ and $\mathbf{H} = (0, H_y, 0)$. Assuming the EM field time dependence as $\mathbf{E}, \mathbf{H} \sim \exp(-i\omega t)$, we represent the Maxwell equations for the TM-polarized wave as

$$\begin{aligned} \frac{\partial E_x^{(m)}}{\partial z} - \frac{\partial E_z^{(m)}}{\partial x} &= \frac{i\omega}{c} H_y^{(m)}, \\ -\frac{\partial H_y^{(m)}}{\partial z} &= -\frac{i\omega}{c} \epsilon_{xx}^{(m)} E_x^{(m)}, \\ \frac{\partial H_y^{(m)}}{\partial x} &= -\frac{i\omega}{c} \epsilon_{zz}^{(m)} E_z^{(m)}. \end{aligned} \quad (1)$$

The superscripts $m = 1, 2, 3, 4, 5$ correspond to the spatial domains $z < -d_{\text{BN}}$, $-d_{\text{BN}} < z < 0$, $0 < z < d_{\text{BN}}$, $d_{\text{BN}} < z < d_{\text{BN}} + d$, and $z > d_{\text{BN}} + d$, respectively. The reason for such separation of the whole space into domains is that inside each domain the dielectric permittivity is homogeneous and generally is described by the diagonal tensor, in the coordinate frame of Fig. 1:

$$\hat{\epsilon}^{(m)} = \begin{pmatrix} \epsilon_{xx}^{(m)} & 0 & 0 \\ 0 & \epsilon_{yy}^{(m)} & 0 \\ 0 & 0 & \epsilon_{zz}^{(m)} \end{pmatrix}.$$

In fact, in the isotropic media the tensor components are the same, for $m = 1$ and $m = 5$ (vacuum) equal to unity, $\epsilon_{xx}^{(1)} = \epsilon_{zz}^{(1)} = \epsilon_{xx}^{(5)} = \epsilon_{zz}^{(5)} = 1$, and for $m = 4$ (isotropic dielectric) $\epsilon_{xx}^{(4)} = \epsilon_{zz}^{(4)} = \epsilon$. The hexagonal boron nitride (spatial domains $m = 2, 3$) is a uniaxial crystal with unequal tensor components in plane and out of plane, with the frequency dependence due to the polar optical phonon response given by

$$\begin{aligned} \epsilon_{xx}^{(2,3)}(\omega) &= \epsilon_{\infty}^{\perp} \left(1 + \frac{\omega_{\text{LO}}^{\perp 2} - \omega_{\text{TO}}^{\perp 2}}{\omega_{\text{TO}}^{\perp 2} - \omega^2 - i\omega\Gamma_{\text{TO}}^{\perp}} \right), \\ \epsilon_{zz}^{(2,3)}(\omega) &= \epsilon_{\infty}^{\parallel} \left(1 + \frac{\omega_{\text{LO}}^{\parallel 2} - \omega_{\text{TO}}^{\parallel 2}}{\omega_{\text{TO}}^{\parallel 2} - \omega^2 - i\omega\Gamma_{\text{TO}}^{\parallel}} \right), \end{aligned} \quad (2)$$

where the transverse (TO) and longitudinal (LO) optical-phonon frequencies for in-plane (out of plane) modes and the corresponding damping parameters Γ are designated by the symbol \perp (\parallel) and their numerical values are (in cm^{-1}) [45] $\omega_{\text{TO}}^{\perp} = 1370$, $\omega_{\text{LO}}^{\perp} = 1610$, $\Gamma_{\text{TO}}^{\perp} = 5$; $\omega_{\text{TO}}^{\parallel} = 780$, $\omega_{\text{LO}}^{\parallel} = 830$, $\Gamma_{\text{TO}}^{\parallel} = 4$. The high-frequency dielectric constants are $\epsilon_{\infty}^{\perp} = 4.87$, $\epsilon_{\infty}^{\parallel} = 2.95$.

Since both the geometry of the structure and the considered wave packet are symmetric with respect to the plane $x = 0$, we can seek the solution of the Maxwell equations (1) in the form of Fourier integrals over $k_x > 0$,

$$\begin{aligned} H_y^{(m)}(x, z) &= \int_0^{\infty} dk_x h_y^{(m)}(k_x, z) \cos(k_x x), \\ E_x^{(m)}(x, z) &= \int_0^{\infty} dk_x e_x^{(m)}(k_x, z) \cos(k_x x), \end{aligned} \quad (3)$$

where $h_y^{(m)}(k_x, z)$ and $e_x^{(m)}(k_x, z)$ are the amplitudes of the k_x th harmonics of the tangential components of the magnetic and electric fields, respectively.

In the semi-infinite medium $m = 1$, the solution of the Maxwell equations can be represented in the matrix form as

$$\begin{pmatrix} h_y^{(1)}(k_x, z) \\ e_x^{(1)}(k_x, z) \end{pmatrix} = \hat{F}_{k_x}^{(1)} \cdot \begin{pmatrix} \mathcal{H}_y^{(1)} \Theta(k_c - k_x) \exp[ip^{(1)}(k_x)(z + d_{\text{BN}})] \\ h_r(k_x) \exp[-ip^{(1)}(k_x)(z + d_{\text{BN}})] \end{pmatrix}. \quad (4)$$

Here

$$\hat{F}_{k_x}^{(1)} = \begin{pmatrix} 1 & 1 \\ \frac{c}{\omega} p^{(1)}(k_x) & -\frac{c}{\omega} p^{(1)}(k_x) \end{pmatrix}$$

is the field matrix, $p^{(1)}(k_x) = \sqrt{(\omega/c)^2 - k_x^2}$ is the wave vector's z component, and $\Theta(k_c - k_x)$ is the Heaviside function. For each line in Eq. (4), if written explicitly, the first term stands for the incident wave packet with the amplitude $\mathcal{H}_y^{(i)}$ and the cutoff in-plane wave vector $k_c < \omega/c$, which propagates in the positive direction of the z axis. Owing to this

restriction, all waves constituting the incident wave packet have real z components of the wave vector. The second term for each line in Eq. (4) is the reflected wave, whose harmonics [with amplitudes $h_r(k_x)$] can be either propagating in the negative direction of the z axis (when $k_x < \omega/c$) or evanescent (when $k_x > \omega/c$) waves. Notice that the sign in the exponent for the evanescent waves is chosen to exclude the harmonics which grows at $z \rightarrow -\infty$. At the same time, in the other semi-infinite spatial domain, $z > d + d_{\text{BN}}$ ($m = 5$), the spectrum consists of transmitted waves only, with $p^{(5)}(k_x) \equiv p^{(1)}(k_x)$,

$$\begin{pmatrix} h_y^{(5)}(k_x, z) \\ e_x^{(5)}(k_x, z) \end{pmatrix} = \begin{pmatrix} 1 \\ \frac{c}{\omega} p^{(5)}(k_x) \end{pmatrix} h_t(k_x) \times \exp[ip^{(5)}(k_x)(z - d_{\text{BN}} - d)]. \quad (5)$$

Again, these transmitted harmonics with amplitudes $h_t(k_x)$ can be either propagating in the positive direction of the z axis or evanescent, decaying for $z \rightarrow +\infty$.

In the finite spatial domain $-d_{\text{BN}} < z < 0$ (medium $m = 2$) the electromagnetic fields will be represented by means of the transfer matrix [46],

$$\hat{Q}_{k_x, z}^{(2)} = \begin{pmatrix} \cos[p^{(2)}(k_x)(z + d_{\text{BN}})] & \frac{i\omega}{c} \frac{\epsilon_{xx}^{(2)}}{p^{(2)}(k_x)} \sin[p^{(2)}(k_x)(z + d_{\text{BN}})] \\ \frac{ic}{\omega} \frac{p^{(2)}(k_x)}{\epsilon_{xx}^{(2)}} \sin[p^{(2)}(k_x)(z + d_{\text{BN}})] & \cos[p^{(2)}(k_x)(z + d_{\text{BN}})] \end{pmatrix},$$

as

$$\begin{pmatrix} h_y^{(2)}(k_x, z) \\ e_x^{(2)}(k_x, z) \end{pmatrix} = \hat{Q}_{k_x, z}^{(2)} \begin{pmatrix} h_y^{(2)}(k_x, -d_{\text{BN}}) \\ e_x^{(2)}(k_x, -d_{\text{BN}}) \end{pmatrix}. \quad (6)$$

Here $p^{(2)}(k_x) = \sqrt{(\omega/c)^2 \epsilon_{xx}^{(2)} - k_x^2 (\epsilon_{xx}^{(2)}/\epsilon_{zz}^{(2)})}$, which is the effective z component of the wave vector in a uniaxial medium [47]. In Eq. (6), we represented the fields in the hBN substrate using values $h_y^{(2)}(k_x, -d_{\text{BN}})$ and $e_x^{(2)}(k_x, -d_{\text{BN}})$ (the EM field tangential components at $z = -d_{\text{BN}}$) as free parameters. This situation is distinct from the case of semi-infinite vacuum [see Eq. (4)], where the amplitudes of the reflected waves were used as free parameters. These free parameters will be eliminated by matching the fields at the interfaces.

In the medium $m = 3$ (spatial domain $0 < z < d_{\text{BN}}$) the field structure is similar to that of Eq. (6) with the following replacement: $p^{(2)} \rightarrow p^{(3)}$ (as a matter of fact, they are the same, i.e., $p^{(3)} = p^{(2)}$), $\epsilon_{xx}^{(2)} \rightarrow \epsilon_{xx}^{(3)}$, $\epsilon_{zz}^{(2)} \rightarrow \epsilon_{zz}^{(3)}$, and

$$\begin{pmatrix} h_y^{(2)}(k_x, -d_{\text{BN}}) \\ e_x^{(2)}(k_x, -d_{\text{BN}}) \end{pmatrix} \rightarrow \begin{pmatrix} h_y^{(3)}(k_x, 0) \\ e_x^{(3)}(k_x, 0) \end{pmatrix}.$$

In other words,

$$\begin{pmatrix} h_y^{(3)}(k_x, z) \\ e_x^{(3)}(k_x, z) \end{pmatrix} = \hat{Q}_{k_x, z}^{(3)} \begin{pmatrix} h_y^{(3)}(k_x, 0) \\ e_x^{(3)}(k_x, 0) \end{pmatrix}, \quad (7)$$

where the transfer matrix is given by

$$\hat{Q}_{k_x, z}^{(3)} = \begin{pmatrix} \cos[p^{(3)}(k_x)z] & \frac{i\omega}{c} \frac{\epsilon_{xx}^{(3)}}{p^{(3)}(k_x)} \sin[p^{(3)}(k_x)z] \\ \frac{ic}{\omega} \frac{p^{(3)}(k_x)}{\epsilon_{xx}^{(3)}} \sin[p^{(3)}(k_x)z] & \cos[p^{(3)}(k_x)z] \end{pmatrix}.$$

In the medium $m = 4$ the situation is quite different because the finite width of this domain in the x direction imposes an additional boundary condition on the slit borders $x = \pm W/2$, namely the vanishing tangential component of the electric field $E_z^{(4)}(\pm W/2, z) = 0$. The solution of the Maxwell equations satisfying these conditions can be expressed as follows:

$$\begin{aligned} E_x^{(4)}(x, z) &= iW \sum_{n=0}^{\infty} v_n \cos \left[\frac{n\pi}{W} \left(x + \frac{W}{2} \right) \right] \\ &\times \{ A_n^{(+)} \exp[iv_n(z - d_{\text{BN}})] \\ &- A_n^{(-)} \exp[-iv_n(z - d_{\text{BN}})] \}, \end{aligned} \quad (8)$$

$$\begin{aligned} H_y^{(4)}(x, z) &= \frac{i\omega\epsilon}{c} W \sum_{n=0}^{\infty} \cos \left[\frac{n\pi}{W} \left(x + \frac{W}{2} \right) \right] \\ &\times \{ A_n^{(+)} \exp[iv_n(z - d_{\text{BN}})] \\ &+ A_n^{(-)} \exp[-iv_n(z - d_{\text{BN}})] \}, \end{aligned} \quad (9)$$

$$\begin{aligned} E_z^{(4)}(x, z) &= \sum_{n=0}^{\infty} n\pi \sin \left[\frac{n\pi}{W} \left(x + \frac{W}{2} \right) \right] \\ &\times \{ A_n^{(+)} \exp[iv_n(z - d_{\text{BN}})] \\ &+ A_n^{(-)} \exp[-iv_n(z - d_{\text{BN}})] \}, \end{aligned} \quad (10)$$

where $v_n = \sqrt{(\frac{\omega}{c})^2 \epsilon - (\frac{n\pi}{W})^2}$.

C. Boundary conditions

The problem in course includes four boundaries between aforementioned spatial domains, at which the fields in the neighboring domains are coupled by matching the boundary conditions. At the surface of the upper hBN layer ($z = -d_{\text{BN}}$, boundary between spatial domains $m = 1$ and $m = 2$) the tangential components of the electric and magnetic fields must be continuous across the interface, i.e.,

$$\begin{aligned} e_x^{(2)}(k_x, -d_{\text{BN}}) &= e_x^{(1)}(k_x, -d_{\text{BN}}), \\ h_y^{(2)}(k_x, -d_{\text{BN}}) &= h_y^{(1)}(k_x, -d_{\text{BN}}). \end{aligned} \quad (11)$$

At the interface between two hBN layers, where graphene layer is arranged ($z = 0$, boundary between media $m = 2$ and $m = 3$) the electric-field tangential component is continuous across the interface, while the magnetic field tangential component is discontinuous due to the presence of two-dimensional currents $j_x(k_x, \omega)$ in graphene,

$$\begin{aligned} e_x^{(2)}(k_x, 0) &= e_x^{(3)}(k_x, 0), \\ h_y^{(3)}(k_x, 0) - h_y^{(2)}(k_x, 0) &= -\frac{4\pi}{c} j_x(k_x, \omega). \end{aligned}$$

Taking into account the Ohm law, $j_x(k_x, \omega) = \sigma(k_x, \omega)e_x^{(2)}(k_x, 0)$ [where $\sigma(k_x, \omega)$ is the conductivity of the graphene, which in the general case will be considered nonlocal [31], i.e., dependent upon the in-plane wave vector k_x], the boundary conditions can be expressed in the matrix form,

$$\begin{pmatrix} h_y^{(3)}(k_x, 0) \\ e_x^{(3)}(k_x, 0) \end{pmatrix} = \hat{Q}_g \begin{pmatrix} h_y^{(2)}(k_x, 0) \\ e_x^{(2)}(k_x, 0) \end{pmatrix} \quad (12)$$

with the matrix

$$\hat{Q}_g = \begin{pmatrix} 1 & -\frac{4\pi}{c}\sigma(k_x, \omega) \\ 0 & 1 \end{pmatrix}.$$

At the surfaces of the PEC film $z = d_{\text{BN}}$ and $z = d_{\text{BN}} + d$ (boundaries between the media $m = 3, 4$ and $m = 4, 5$, respectively) the situation is more complicated. The tangential component of the magnetic field is continuous across the interfaces over the slit area,

$$H_y^{(3)}(x, d_{\text{BN}}) = H_y^{(4)}(x, d_{\text{BN}}), \quad -\frac{W}{2} \leq x \leq \frac{W}{2},$$

$$H_y^{(5)}(x, d_{\text{BN}} + d) = H_y^{(4)}(x, d_{\text{BN}} + d), \quad -\frac{W}{2} \leq x \leq \frac{W}{2}. \quad (13)$$

The tangential component of the electric field also has to be continuous across the interfaces at the slit area and should vanish beyond the slit because the metal is assumed perfect. Therefore, boundary conditions can be expressed by the formulas

$$E_x^{(3)}(x, d_{\text{BN}}) = \begin{cases} E_x^{(4)}(x, d_{\text{BN}}), & -\frac{W}{2} \leq x \leq \frac{W}{2}, \\ 0, & \text{otherwise} \end{cases},$$

$$E_x^{(5)}(x, d_{\text{BN}} + d) = \begin{cases} E_x^{(4)}(x, d_{\text{BN}} + d), & -\frac{W}{2} \leq x \leq \frac{W}{2}, \\ 0, & \text{otherwise} \end{cases}. \quad (14)$$

It should be pointed out that, due to the fact that we use different bases of eigenfunctions in medium $m = 4$ and in media $m = 3$ and $m = 5$, the boundary conditions (13) and (14) cannot be written in the same way as at boundaries $z = 0$ and $z = -d_{\text{BN}}$ where they could be expressed separately for each spatial harmonic, $e_x^{(m)}(k_x, z)$ and $h_y^{(m)}(k_x, z)$. Equations (13) and (14) involve the total fields in each point x , $E_x^{(m)}(x, z)$, $H_y^{(m)}(x, z)$, and involve all k_x harmonics. In other words, these relations are integral equations. However, they can be discretized using the specific form of the fields inside the slit, Eqs. (8) and (9).

D. Amplitudes of the eigenmodes inside the slit

Applying consequently boundary conditions (11) and (12) [jointly with expressions (4)–(7) for the fields in media $m = 1, 2, 3$] one can obtain expressions for the electromagnetic field tangential components of each harmonic as

$$\begin{pmatrix} h_y^{(3)}(k_x, d_{\text{BN}}) \\ e_x^{(3)}(k_x, d_{\text{BN}}) \end{pmatrix} = \hat{F}_{k_x}^{(\text{tot})} \begin{pmatrix} \mathcal{H}_y^{(i)} \Theta(k_c - k_x) \\ h_r(k_x) \end{pmatrix}, \quad (15)$$

where the total field matrix $\hat{F}_{k_x}^{(\text{tot})}$ composed from the transfer matrices of media $m = 2, 3$, boundary condition matrix across the graphene, and the field matrix in medium $m = 1$ is

$$\hat{F}_{k_x}^{(\text{tot})} = \hat{Q}_{k_x, d_{\text{BN}}}^{(3)} \hat{Q}_g \hat{Q}_{k_x, 0}^{(2)} \hat{F}_{k_x}^{(1)}. \quad (16)$$

Substituting Eqs. (5), (8), (9), and (15) into boundary conditions (13) and (14) and using orthogonality relations between the x dependence of the fields in the slit, Eqs. (8) and (9), and the k_x harmonics [48], it is possible to obtain equations for the amplitudes of forward- and backward-propagating modes inside the slit, $A_{2n'}^{(+)}$ and $A_{2n'}^{(-)}$:

$$\begin{aligned} & \frac{W}{2} \frac{i\omega\epsilon}{c} (1 + \delta_{n',0}) [A_{2n'}^{(+)} + A_{2n'}^{(-)}] \\ & - i \frac{W^2}{2\pi} \sum_{n=0}^{\infty} v_{2n} [A_{2n}^{(+)} - A_{2n}^{(-)}] \tilde{I}_{2n', 2n}(\omega) \\ & = -2 \frac{c}{\omega} \mathcal{H}_y^{(i)} \int_0^{\infty} dk_x \mathcal{P}_{2n' || k_x} \Theta(k_c - k_x) \frac{P^{(1)}(k_x)}{[\hat{F}_{k_x}^{(\text{tot})}]_{22}}; \quad (17) \\ & \frac{\epsilon}{2} (1 + \delta_{n',0}) \times [A_{2n'}^{(+)} \exp(iv_{2n'}d) + A_{2n'}^{(-)} \exp(-iv_{2n'}d)] \\ & - \frac{W}{2\pi} \sum_{n=0}^{\infty} v_{2n} I_{2n', 2n}(\omega) \\ & \times [A_{2n}^{(+)} \exp(iv_{2n}d) - A_{2n}^{(-)} \exp(-iv_{2n}d)] = 0, \quad (18) \end{aligned}$$

where

$$\begin{aligned} \mathcal{P}_{2n' || k_x} &= \frac{2}{W} \int_0^{W/2} dx \cos \left[\frac{2n'\pi}{W} \left(x + \frac{W}{2} \right) \right] \cos [k_x x] \\ &= \frac{2}{W} \frac{k_x \sin \left[k_x \frac{W}{2} \right]}{k_x^2 - \left(\frac{2n'\pi}{W} \right)^2}, \end{aligned} \quad (19)$$

$$\tilde{I}_{2n', 2n}(\omega) = 2 \int_0^{\infty} dk_x \mathcal{P}_{2n' || k_x} \mathcal{P}_{2n || k_x} \frac{[\hat{F}_{k_x}^{(\text{tot})}]_{12}}{[\hat{F}_{k_x}^{(\text{tot})}]_{22}}$$

and

$$I_{2n',2n}(\omega) = 2 \int_0^\infty dk_x \frac{\mathcal{P}_{2n' || k_x} \mathcal{P}_{2n || k_x}}{p^{(5)}(k_x)}.$$

The system of equations (17) and (18) was solved by truncating it to a sufficiently large order, n and checking the convergence. Once the amplitudes $A_{2n}^{(\pm)}$ have been found, the observable properties such as reflectance and transmittance are calculated in a straightforward way [48].

III. SUSPENDED GRAPHENE

In order to clarify the influence of the graphene sheet on the transmittance and reflectance of the structure of Fig. 1 we consider first the situation where the slit is not filled ($\epsilon = 1$) and both hBN layers are absent. In other words, the graphene layer is deposited directly on the metal film and is suspended at the area of the slit. Equations describing this case can be obtained from general ones, Eqs. (17) and (18), by setting equal to zero the thickness of both hBN layers, $d_{\text{BN}} = 0$. Then total field matrix (16) is written in a simpler form, namely,

$$\hat{F}_{k_x}^{(\text{tot})} = \hat{Q}_g \hat{F}_{k_x}^{(1)} = \begin{pmatrix} 1 - \frac{4\pi}{\omega} \sigma(k_x, \omega) p^{(1)}(k_x) & 1 + \frac{4\pi}{\omega} \sigma(k_x, \omega) p^{(1)}(k_x) \\ \frac{c}{\omega} p^{(1)}(k_x) & -\frac{c}{\omega} p^{(1)}(k_x) \end{pmatrix}.$$

As a consequence, Eq. (17) can be rewritten as

$$\begin{aligned} & \frac{W}{2} \frac{i\omega\epsilon}{c} (1 + \delta_{n',0}) [A_{2n'}^{(+)} + A_{2n'}^{(-)}] \\ & + i \frac{W^2}{2\pi} \frac{\omega}{c} \sum_{n=0}^{\infty} v_{2n} [A_{2n}^{(+)} - A_{2n}^{(-)}] J_{2n',2n}(\omega) \\ & = (-1)^n \frac{2\mathcal{H}_y^{(i)}}{W} \left[\text{Si} \left(\frac{k_c W}{2} + n'\pi \right) + \text{Si} \left(\frac{k_c W}{2} - n'\pi \right) \right], \end{aligned} \quad (20)$$

where

$$\begin{aligned} J_{2n',2n}(\omega) &= 2 \int_0^\infty dk_x \frac{\mathcal{P}_{2n' || k_x} \mathcal{P}_{2n || k_x}}{p^{(1)}(k_x)} \\ &\times \left[1 + \frac{4\pi}{\omega} \sigma(k_x, \omega) p^{(1)}(k_x) \right], \end{aligned}$$

and $\text{Si}(x)$ is the integral sine function. As a result, the system with suspended graphene is described by Eqs. (18) and (20) with $\epsilon = 1$. Notice that when the graphene is considered within the local approximation (neglecting spatial dispersion of the conductivity), integrals $I_{2n',2n}(\omega)$ and $J_{2n',2n}(\omega)$ can be calculated semianalytically [48], which considerably reduces the time of numerical calculation.

The spatial shape of the incoming wave packet can be obtained from Eqs. (3) and (4) and expressed in the form

$$H_y^{(i)}(x, 0) = \mathcal{H}_y^{(i)} \frac{\sin(k_c x)}{x}. \quad (21)$$

This dependence is depicted in Fig. 2(a). It can be seen that a larger spectral width k_c (solid line) corresponds to a more focused beam in real space. The respective width of the wave packet in real space $\ell = 2\pi/k_c$ can be obtained from Eq. (21)

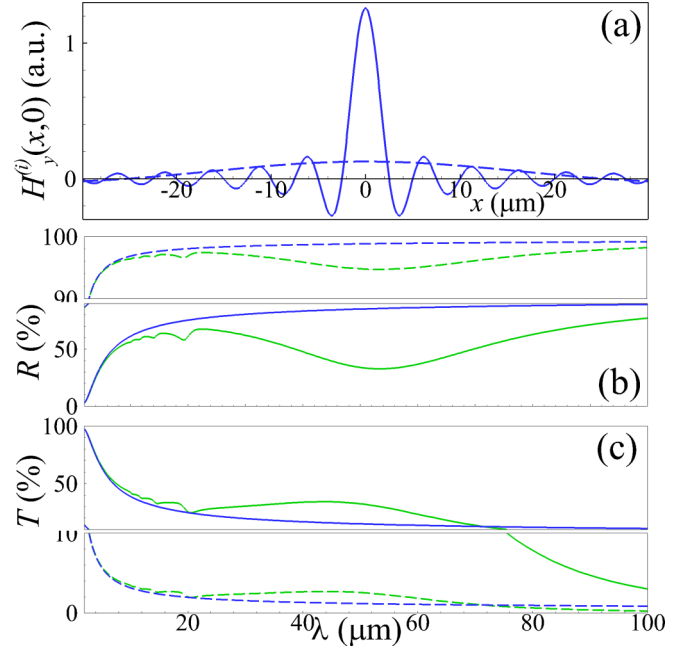


FIG. 2. (a) Examples of spatial shape of the incident wave packet $H_y^{(i)}(x, 0)$ for $\lambda = 5 \mu\text{m}$ and two values of the spectral width, $ck_c/\omega = 1$ (solid line) and $ck_c/\omega = 0.1$ (dashed line); (b),(c) reflectance R (b) and transmittance T (c) of graphene monolayer suspended over the slit for two values of the wave-packet spectral width: $ck_c/\omega = 1$ (solid lines) and $ck_c/\omega = 0.1$ (dashed lines). Other parameters of the structure are $d = 100 \text{ nm}$, $W = 1.5 \mu\text{m}$, $\gamma = 7.5 \text{ meV}$, $E_F = 0 \text{ eV}$ (blue lines), $E_F = 0.3 \text{ eV}$ (green lines).

by using the condition $H_y^{(i)}(\pm\ell/2, 0) = 0$. As a consequence, the narrower beam (with larger k_c) exhibits a lower reflectance R and a higher transmittance T [compare dashed and solid lines in Figs. 2(b) and 2(c)], because a larger fraction of the incident wave's energy flux penetrates the slit, thus avoiding the diffraction on its edges. In Fig. 2 and throughout the reminder of the paper we represent wave packet's frequency ω in terms of the corresponding wavelength in the vacuum, $\lambda = 2\pi c/\omega$. Also, in all figures we will assume that the relation between k_c and the wave vector ω/c is fixed for each frequency, i.e., the value $\xi = \lambda k_c/(2\pi)$ is kept constant. Therefore, the wave packet's width in real space depends upon the wavelength as $\ell = \lambda/\xi$. In the situation of the bare slit [$E_F = 0$, blue lines in Figs. 2(b) and 2(c)] an increase of the wavelength λ leads to a growth of the reflectance R [see Fig. 2(b)] and a decrease of the transmittance T [see Fig. 2(c)]. This phenomenon can be accounted for by the essentially subwavelength character of the wave-packet diffraction. In fact, in the frequency range of Fig. 2 all the wavelengths of the wave packet are larger than the slit width. At the same time, for a larger ratio between the wavelength and the slit width, the presence of the slit exerts less influence on the diffraction process, thus the reflectance becomes more like that from a homogeneous PEC film, i.e., it increases to unity with the simultaneous decrease of the transmittance. When the slit is covered by doped graphene [$E_F = 0.3 \text{ eV}$, green lines in Figs. 2(b) and 2(c)], the aforementioned growth of the reflectance and decrease of the transmittance is nonmonotonic, demonstrating a series of

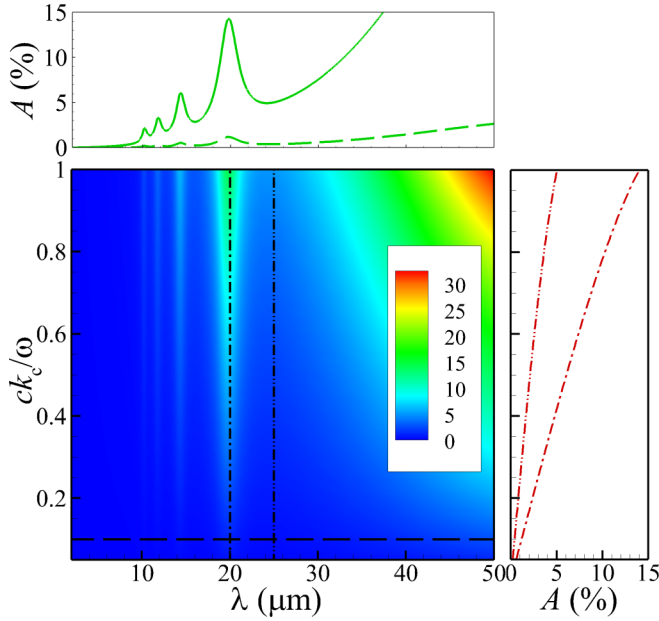


FIG. 3. Absorbance A vs wavelength λ , and spectral width of the wave packet k_c (left bottom panel) for doped graphene with $E_F = 0.3$ eV suspended on top of the slit. The top panel shows the absorbance for two fixed values of the spectral width, $ck_c/\omega = 0.1$ (dashed line, the dependence is taken along the corresponding dashed horizontal line in the left bottom panel) and $ck_c/\omega = 1$ (solid line, the dependence is taken along the upper edge of the left bottom panel). Right bottom panel shows the absorbance (horizontal axis) vs spectral width (vertical axis) for two fixed values of wavelength $\lambda = 20 \mu\text{m}$ (dashed-and-dotted line) and $\lambda = 25 \mu\text{m}$ (dashed-and-double-dotted line). These dependencies are taken along the correspondent vertical dashed-and-dotted and dashed-and-double-dotted lines in the left bottom panel. The other parameters are the same as in Fig. 2.

local minima. One of these minima of the reflectance near $\lambda \approx 55 \mu\text{m}$ (and the corresponding maximum of the transmittance) takes place owing to the Drude absorbance in graphene. At the same time, other reflectance minima below $\lambda \lesssim 20 \mu\text{m}$ are due to excitation of SPPs in graphene, as it will be shown below.

Quite interesting are the absorption spectra of the considered structure. As can be seen from the top panel of Fig. 3, the absorbance, $A = 1 - R - T$, is high at the wavelengths corresponding to the reflectance and transmittance minima. Furthermore, a larger spectral width of the incident wave packet (k_c) increases absorbance [see right bottom panel in Fig. 3], because the wave packet becomes narrower in real space, and the larger part of the incoming power interacts with the suspended graphene. Also, the larger spectral width of the incident wave packet makes these absorbance peaks more pronounced [see left bottom panels of Fig. 3], while their positions (wavelengths λ) are not affected. At the same time, the positions of the absorption peaks are strongly influenced by the graphene's Fermi energy [see Fig. 4(a)]. This fact resembles the crucial property of graphene SPPs whose dispersion curve $\omega(k_x)$ scales with the Fermi energy approximately as $\omega \propto \sqrt{k_x E_F}$ for small k_x . A more detailed analysis leads to the following expression for the characteristic frequencies of

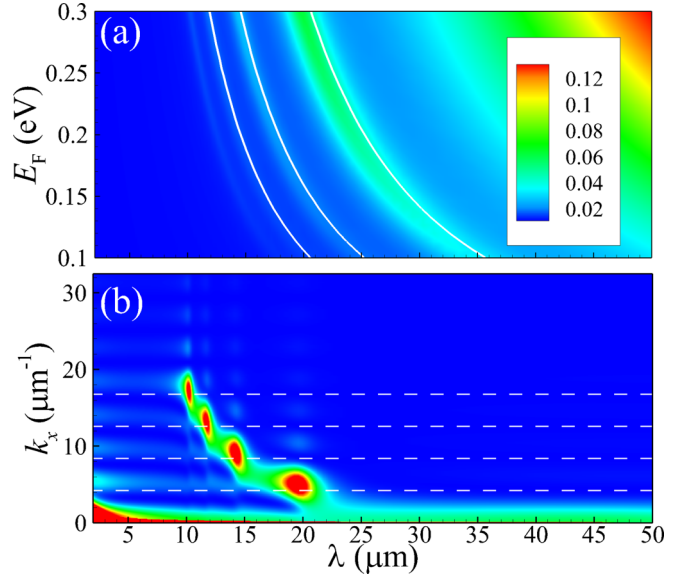


FIG. 4. (a) Absorbance A (depicted by color map) vs wavelength λ and graphene's Fermi energy E_F ; (b) amplitude of the electric field of the reflected wave harmonics $|cp^{(1)}(k_x)h_r(k_x)/\omega|$ vs the wavelength and the wave vector k_x for the fixed Fermi energy $E_F = 0.3$ eV. In all panels $ck_c/\omega = 0.5$, while other parameters are the same as in Fig. 2. Solid white lines [superimposed on the color map in (a)] demonstrate the SPP eigenmodes with the wave vectors $k_x^{(n)} = 2n\pi/W$ ($n = 1, 2, 3$, from right to left); the same wave vectors are depicted in (b) by white dashed horizontal lines.

the SPP eigenmodes:

$$\omega_n = \frac{\sqrt{2}\alpha E_F}{\hbar} \times \left(\sqrt{1 + \left(\frac{2n\pi\hbar c}{\alpha E_F W} \right)^2} - 1 \right)^{1/2}, \quad (22)$$

where $n = 1, 2, 3, \dots$ and α stands for the fine-structure constant. Note that Eq. (22) yields the above-mentioned square-root dependence upon the SPP eigenmode wave vector, $k_x^{(n)} = 2\pi n/W$, if $k_x^{(n)}c \ll \alpha E_F$. These modes (represented in terms of $\lambda_n = 2\pi c/\omega_n$) are depicted as the white solid lines in Fig. 4(a). The polaritonic character of the absorption peaks is confirmed by the fact that the spectral positions of the absorbance maxima coincide with the graphene SPP eigenmodes. [49] Moreover, the modulus of the electric field of the reflected wave harmonics [depicted in Fig. 4(b)] has its maxima near the resonance frequencies ω_n [Eq. (22)]. The associated wave vectors $k_x^{(n)}$ [horizontal dashed lines in Fig. 4(b)] correspond to the symmetric spatial profiles of the tangential components of the eigenmode's electromagnetic field inside the slit [see Eqs. (8) and (9)]. In other words, when the incident wave packet's frequency coincides with that of an SPP eigenmode with the wave vector $k_x^{(n)} = 2\pi n/W$, the wave packet, being diffracted on the slit, resonantly excites SPPs in graphene. The magnitude of these resonant features decreases with n as it can be seen from Eq. (20) where the right-hand side tends to zero for large n' . Such a polariton, owing to multiple reflections from the slit edges, forms a standing wave

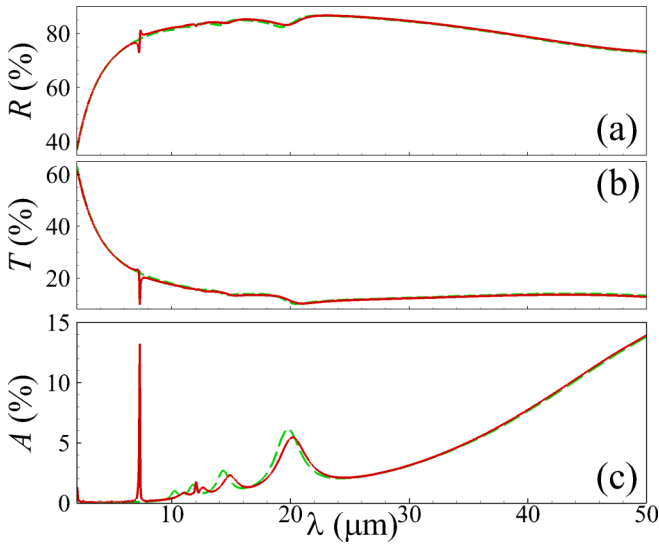


FIG. 5. Reflectance (a), transmittance (b), and absorbance (c) of (i) suspended graphene layer (dashed green lines) and (ii) graphene layer cladded by two hBN layers with thicknesses $d_{\text{BN}} = 1$ nm (solid red lines). In both cases $E_F = 0.3$ eV and the incident wave packet is characterized by the spectral width $ck_c/\omega = 0.5$. Other parameters are the same as in Fig. 2.

in the suspended graphene with the nodes of its electric field (x component) at the edges of the slit. This resonant excitation leads to the transformation of incident wave packet's energy into the energy of the SPP standing wave; this phenomenon gives rise to the resonant absorption. Qualitatively, the situation here is similar to the light absorption in a structure composed of nonabsorbing nanoparticles (NPs) deposited on a homogeneous graphene sheet, where the symmetry breaking caused by the NPs induces surface plasmon polaritons and originates absorption of propagating EM waves due to energy dissipation by the graphene plasmons [50]. Indeed, the absorbance spectra of Fig. 2 show a similarity to that of the “graphene + NPs” system [50], although here we observe not just the lowest energy (longest wavelength) absorption peak but also its overtones according to Eq. (22).

IV. EFFECT OF THE SUBSTRATE

The essential physics behind the optical properties of the graphene-covered slit has been established in the previous section and now we may address a further question: How will the results change if the graphene is not deposited directly on the metal film but rather cladded by two hBN layers as depicted in Fig. 1? To answer this question, in Fig. 5 we present a comparison of the reflectance, transmittance, and absorbance of the suspended (dashed green lines) and hBN-encapsulated graphene (solid red lines) [51]. Results for the hBN-encapsulated graphene were obtained by solving the system of equations (17) and (18) employing numerical integration of $\tilde{I}_{2n',2n}(\omega)$. As can be seen from the comparison of the dashed and solid lines in Fig. 5, the presence of hBN leads to the small shift of the positions of the SPP absorbance maxima, and the appearance of two additional

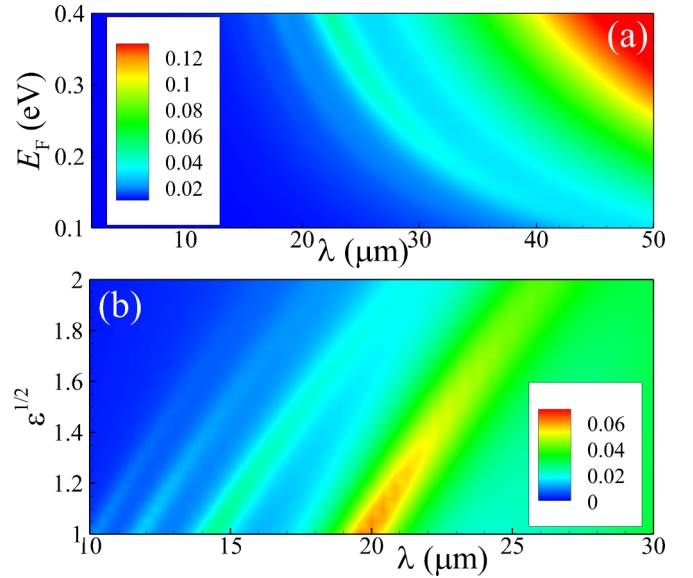


FIG. 6. (a) Absorbance A vs wavelength λ and Fermi energy E_F for the slit filled by a dielectric with $\epsilon = 3.9$; (b) absorbance vs wavelength and refractive index $\epsilon^{1/2}$ for the graphene Fermi energy $E_F = 0.3$ eV. In both panels $ck_c/\omega = 0.5$ and all other parameters are the same as in Fig. 2.

maxima (nearly $\lambda \approx 7.3$ μm and $\lambda \approx 12$ μm) due to the excitation of optical phonons in the hBN cladding layers.

One of the crucial properties of SPPs is the strong sensitivity of their dispersion to the dielectric constants of the surrounding media, which should also apply to the dielectric filling the slit in the present case. Therefore, Fig. 6(a) presents the absorbance of the graphene layer deposited over the slit filled by a material with the dielectric constant $\epsilon = 3.9$. As it follows from the comparison of Figs. 6(a) and 4(a), the presence of the dielectric inside the slit results in a redshift of the plasmonic absorption peaks. In more detail this phenomenon is demonstrated in Fig. 6(b). As it can be seen from this plot, there is an almost linear dependence of the plasmonic absorption peak positions upon the refractive index $\epsilon^{1/2}$. Even more, when the refractive index is changed in the limits between 1 and 2, the plasmonic absorption peak wavelength is shifted by ~ 5 μm .

This phenomenon can be used in plasmonic sensors. The advantage of the graphene-based plasmonic sensor is an additional degree of its dynamical tunability. Thus, if a source of electromagnetic radiation with a fixed wavelength is used, then the position of the plasmonic absorption peak can be tuned to the desired wavelength by adjusting the graphene's Fermi energy and its value can provide information about the dielectric constant of the medium that fills the slit.

V. CONCLUSION

To conclude, we considered the diffraction of the spatially localized wave packet on the single slit in a perfect metallic film covered by monolayer graphene. We have shown that this geometry is suitable for the excitation of surface plasmon polaritons in graphene. The diffraction of the wave packet on the slit is accompanied by the excitation of the polariton

standing wave, for which the vertical edges of the slit in the PEC serve as a cavity. The resonance condition for the excitation of such standing waves can be expressed in the following manner: the excitation of SPPs takes place for a given frequency of the incident wave packet ω , if the slit width contains an integer number of the polariton wavelengths, $\lambda = 2\pi/k_x$, where k_x is the SPP wave vector for the frequency ω .

The excitation of SPPs is manifested by the appearance of the peaks in the absorbance spectrum. These features become detectable if the wave packet is sufficiently narrow in real space (that is, for $ck_c/\omega \sim 1$) as shown in Fig. 2. We believe that such a wave packet can be obtained from a Gaussian beam by using a cylindrical lens located in the far field for focusing the beam precisely onto the system's surface and a slit diaphragm eventually can be used to remove Gaussian beam tails beyond the cut wave vector k_c , which was not considered here. We notice that in the case of other shapes of the wave packet (as well as the monochromatic plane wave) the results will be qualitatively the same. The positions of the resonant absorption peaks can be effectively tuned by

the electrostatic gating of graphene. The resonant frequencies are shown to be very sensitive to the refractive index of the medium, which fills the slit. This phenomenon can be used for environment sensing. The advantage of such a graphene-based sensor is the possibility to tune (by the graphene gating) the position of the absorption peaks to the spectral range where the fingerprints of the molecules are the most intense, e.g., due to the presence of dipolar vibration modes.

ACKNOWLEDGMENTS

The authors are grateful for useful discussions with H. Crespo. The authors acknowledge support from the European Commission through the project "Graphene- Driven Revolutions in ICT and Beyond" (Ref. No. 881603), and the Portuguese Foundation for Science and Technology through the Strategic Funding UID/FIS/04650/2019. Additionally, the authors acknowledge financing from FEDER and the Portuguese Foundation for Science and Technology (FCT) through Project No. POCI-01-0145-FEDER-028114.

-
- [1] R. Wood, *Philos. Mag.* **4**, 396 (1902).
 [2] L. Rayleigh, *Proc. R. Soc. London, Ser. A* **79**, 399 (1907).
 [3] T. W. Ebbesen, H. J. Lezec, H. F. Ghaemi, T. Thio, and P. A. Wolff, *Nature (London)* **391**, 667 (1998).
 [4] J. A. Porto, F. J. García-Vidal, and J. B. Pendry, *Phys. Rev. Lett.* **83**, 2845 (1999).
 [5] B. Sturman, E. Podivilov, and M. Gorkunov, *Phys. Rev. B* **84**, 205439 (2011).
 [6] A. A. Maradudin, I. Simonsen, J. Polanco, and R. M. Fitzgerald, *J. Opt.* **18**, 024004 (2016).
 [7] B. Sturman, E. Podivilov, and M. Gorkunov, *Phys. Rev. B* **82**, 115419 (2010).
 [8] J.-W. Li, J.-S. Hong, W.-T. Chou, D.-J. Huang, and K.-R. Chen, *Plasmonics* **13**, 2249 (2018).
 [9] Y. Takakura, *Phys. Rev. Lett.* **86**, 5601 (2001).
 [10] F. Yang and J. R. Sambles, *Phys. Rev. Lett.* **89**, 063901 (2002).
 [11] J. Bravo-Abad, L. Martín-Moreno, and F. J. García-Vidal, *Phys. Rev. E* **69**, 026601 (2004).
 [12] T. Park, S. Kang, and H. Eom, *IEEE Trans. Antennas Propag.* **42**, 112 (1994).
 [13] T. H. Isaac, J. Gómez Rivas, J. R. Sambles, W. L. Barnes, and E. Hendry, *Phys. Rev. B* **77**, 113411 (2008).
 [14] S.-H. Chang and Y.-L. Su, *J. Opt. Soc. Am. B* **32**, 38 (2015).
 [15] S.-H. Chang and Y.-L. Su, *J. Opt. Soc. Am. B* **32**, 45 (2015).
 [16] W. L. Barnes, A. Dereux, and T. W. Ebbesen, *Nature (London)* **424**, 824 (2003).
 [17] Y. V. Bludov, A. Ferreira, N. M. R. Peres, and M. I. Vasilevskiy, *Int. J. Mod. Phys. B* **27**, 1341001 (2013).
 [18] F. J. García de Abajo, *ACS Photon.* **1**, 135 (2014).
 [19] T. Low and P. Avouris, *ACS Nano* **8**, 1086 (2014).
 [20] S. Xiao, X. Zhu, B.-H. Li, and N. A. Mortensen, *Front. Phys.* **11**, 117801 (2016).
 [21] P.-Y. Chen, C. Argyropoulos, M. Farhat, and J. S. Gomez-Diaz, *Nanophotonics* **6**, 1239 (2017).
 [22] X. Luo, T. Qiu, W. Lu, and Z. Ni, *Mater. Sci. Eng., R* **74**, 351 (2013).
 [23] A. Y. Nikitin, F. Guinea, F. J. García-Vidal, and L. Martín-Moreno, *Phys. Rev. B* **84**, 195446 (2011).
 [24] F. H. L. Koppens, D. E. Chang, and F. J. García de Abajo, *Nano Lett.* **11**, 3370 (2011).
 [25] A. Principi, R. Asgari, and M. Polini, *Solid State Commun.* **151**, 1627 (2011).
 [26] X. Gu, I.-T. Lin, and J.-M. Liu, *Appl. Phys. Lett.* **103**, 071103 (2013).
 [27] P. Alonso-González, A. Y. Nikitin, Y. Gao, A. Woessner, M. B. Lundeberg, A. Principi, N. Forcellini, W. Yan, S. Vélez, A. J. Huber, K. Watanabe, T. Taniguchi, F. Casanova, L. E. Hueso, M. Polini, J. Hone, F. H. L. Koppens, and R. Hillenbrand, *Nat. Nanotechnol.* **12**, 31 (2016).
 [28] A. Principi, E. van Loon, M. Polini, and M. I. Katsnelson, *Phys. Rev. B* **98**, 035427 (2018).
 [29] N. J. M. Horing, A. Iurov, G. Gumbs, A. Politano, and G. Chiarello, in *Low-Dimensional and Nanostructured Materials and Devices*, edited by H. Ünlü, N. J. M. Horing, and J. Dabrowski, (Springer, Cham, 2016), pp. 351–400.
 [30] D. Alcaraz Iranzo, S. Nanot, E. J. C. Dias, I. Epstein, C. Peng, D. K. Efetov, M. B. Lundeberg, R. Parret, J. Osmond, J.-Y. Hong, J. Kong, D. R. Englund, N. M. R. Peres, and F. H. L. Koppens, *Science* **360**, 291 (2018).
 [31] E. J. C. Dias, D. A. Iranzo, P. A. D. Gonçalves, Y. Hajati, Y. V. Bludov, A.-P. Jauho, N. A. Mortensen, F. H. L. Koppens, and N. M. R. Peres, *Phys. Rev. B* **97**, 245405 (2018).
 [32] F. H. L. Koppens, R. Asgari, M. Polini, T. Taniguchi, J. Hone, M. B. Lundeberg, R. Hillenbrand, Y. Gao, M. Autore, K. Watanabe, A. Woessner, B. Van Duppen, P. Alonso-González, and C. Tan, *Science* **357**, 187 (2017).
 [33] Z. Q. Li, E. A. Henriksen, Z. Jiang, Z. Hao, M. C. Martin, P. Kim, H. L. Stormer, and D. N. Basov, *Nature Physics* **4**, 532 (2008).
 [34] L. Ju, B. Geng, J. Horng, C. Girit, M. Martin, Z. Hao, H. A. Bechtel, X. Liang, A. Zettl, Y. R. Shen, and F. Wang, *Nat. Nanotechnol.* **6**, 630 (2011).

- [35] Y. Yao, M. A. Kats, R. Shankar, Y. Song, J. Kong, M. Loncar, and F. Capasso, *Nano Lett.* **14**, 214 (2014).
- [36] Z. Fei, A. S. Rodin, G. O. Andreev, W. Bao, A. S. McLeod, M. Wagner, L. M. Zhang, Z. Zhao, M. Thiemens, G. Dominguez, M. M. Fogler, A. H. Castro Neto, C. N. Lau, F. Keilmann, and D. N. Basov, *Nature (London)* **487**, 82 (2012).
- [37] J. Chen, M. Badioli, P. Alonso-González, S. Thongrattanasiri, F. Huth, J. Osmond, M. Spasenović, A. Centeno, A. Pesquera, P. Godignon, A. Z. Elorza, N. Camara, F. J. García de Abajo, R. Hillenbrand, and F. H. L. Koppens, *Nature (London)* **487**, 77 (2012).
- [38] P. Alonso-Gonzalez, A. Y. Nikitin, F. Golmar, A. Centeno, A. Pesquera, S. Velez, J. Chen, G. Navickaite, F. Koppens, A. Zurutuza, F. Casanova, L. E. Hueso, and R. Hillenbrand, *Science* **344**, 1369 (2014).
- [39] E. J. Dias and N. M. Peres, *ACS Photon.* **4**, 3071 (2017).
- [40] J. N. Anker, W. P. Hall, O. Lyandres, N. C. Shah, J. Zhao, and R. P. Van Duyne, *Nat. Mater.* **7**, 442 (2008).
- [41] Y. Huang, S. Zhong, H. Yao, and D. Cui, *Phys. Status Solidi A* **214**, 1600550 (2017).
- [42] B. Meshginqalam, M. T. Ahmadi, R. Ismail, and A. Sabatyan, *Plasmonics* **12**, 1991 (2017).
- [43] H. Hu, X. Yang, F. Zhai, D. Hu, R. Liu, K. Liu, Z. Sun, and Q. Dai, *Nat. Commun.* **7**, 12334 (2016).
- [44] M. Born and E. Wolf, *Principles of Optics* (Pergamon, Oxford, 1980).
- [45] A. Kumar, T. Low, K. H. Fung, P. Avouris, and N. X. Fang, *Nano Lett.* **15**, 3172 (2015).
- [46] M. F. Cerqueira, L. G. Vieira, A. Alves, R. Correia, M. Huber, A. Andreev, A. Bonanni, and M. I. Vasilevskiy, *J. Phys. D: Appl. Phys.* **50**, 365103 (2017).
- [47] T. Dumelow, T. Parker, S. Smith, and D. Tilley, *Surf. Sci. Rep.* **17**, 151 (1993).
- [48] See Supplemental Material at <http://link.aps.org/supplemental/10.1103/PhysRevB.101.075415> for details on orthogonality of eigenfunctions inside and outside the slit, reflectance and transmittance calculation, and calculation of integral.
- [49] The values of λ_n given by Eq. (22) and the computed absorbance maxima [Fig. 4(a)] do not coincide exactly, which is probably related to the known problem of describing steplike functions by Fourier integrals, the so-called Gibbs phenomenon. With considerably more terms in the numerical solution we could obtain a better agreement.
- [50] J. E. Santos, M. I. Vasilevskiy, N. M. R. Peres, G. Smirnov, and Y. V. Bludov, *Phys. Rev. B* **90**, 235420 (2014).
- [51] Results for the hBN-encapsulated graphene were obtained by solving the system of equations (17) and (18) employing numerical integration of $\tilde{I}_{2n', 2n}(\omega)$.